Robust optimal design of diffusion-weighted magnetic resonance experiments for skin microcirculation

J. Choi [a,b,*], L.G. Raguin [a,c]

[a] Department of Mechanical Engineering, Michigan State University, East Lansing, MI 48824-1226, USA
[b] Department of Electrical & Computer Engineering, Michigan State University, East Lansing, MI 48824-1226, USA
[c] Department of Radiology, Michigan State University, East Lansing, MI 48824-1313, USA

ARTICLE INFO

ABSTRACT

Skin microcirculation plays an important role in several diseases including chronic venous insufficiency and diabetes. Magnetic resonance (MR) has the potential to provide quantitative information and a better penetration depth compared with other non-invasive methods such as laser Doppler flowmetry or optical coherence tomography. The continuous progress in hardware resulting in higher sensitivity must be coupled with advances in data acquisition schemes. In this article, we first introduce a physical model for quantifying skin microcirculation using diffusion-weighted MR (DWMR) based on an effective dispersion model for skin leading to a q-space model of the DWMR complex signal, and then design the corresponding robust optimal experiments. The resulting robust optimal DWMR protocols improve the worst-case quality of parameter estimates using nonlinear least squares optimization by exploiting available *a priori* knowledge of model parameters. Hence, our approach optimizes the gradient strengths and directions used in DWMR experiments to robustly minimize the size of the parameter estimation error with respect to model parameter uncertainty. Numerical evaluations are presented to demonstrate the effectiveness of our approach as compared to conventional DWMR protocols.

1. Introduction

Skin can be thought of as the first line of defense of the body against pathogens found in the environment. From outermost to innermost layer, the skin possesses three primary layers, as shown in Fig. 1: the epidermis (with a thickness ranging from 0.05 mm on the eyelids to 1.5 mm on the palms and soles), the dermis (from 0.3 mm on the eyelids and 3.0 mm on the back), and the hypodermis. Nourishment and waste removal in the dermis are accomplished through the blood vessels present in the dermis, which also provide the same service to the cells in the deepest layers of the epidermis (Stratum basale) via diffusion. These blood vessels are composed of capillaries, arterioles, venules, and arteriovenous anastomosis (shunting vessels). The former are used for nutrition, while perfusion through the latter three allows for temperature regulation and feeding and draining of the capillary network [1]. Diseases such as chronic venous insufficiency [2] and diabetes [3] impair skin perfusion, which may lead to decubitus ulcer formations and necrosis. In wound healing, vascular supply to the wound is essential and relies on neovascularization or angiogenesis [4], and means of quantitatively characterizing perfusion is crucial for prognosis.

In vivo skin studies using nuclear magnetic resonance (NMR) spectroscopy and imaging offer several advantages over optical techniques such as laser Doppler flowmetry (LDF, see [5,1]) and optical coherence tomography (OCT, see [6–9]). Namely, there is no limitation of the depth of the field-of-view (FOV), and, while LDF data compound effects from flow, density of light scatterers, and depth-of FOV and are reported in arbitrary units, NMR protocols can be quantitative [10]. Wright et al. [11] provide a review of non-invasive methods for evaluating the skin's microcirculation, wherein specific advantages and disadvantages for all available methods are presented. In particular, LDF suffers from large day-to-day variance (on the order of 20%). Wright et al. discuss two additional experimental techniques used to measure skin microcirculation: laser Doppler perfusion imaging and photoplethysmography, however the former is scantly used and requires more validation studies and the latter suffers from the same shortcomings as LDF. Finally, this review points out that "the use of MRI as a dermatological tool for inspecting and quantifying the skin is only considered to be at a preliminary stage".

For skin studies, MRI suffers from low signal-to-noise ratios (SNR) due to the relatively low relaxation times compared to other tissues: T_1 values for the different skin layers varies from 135 to
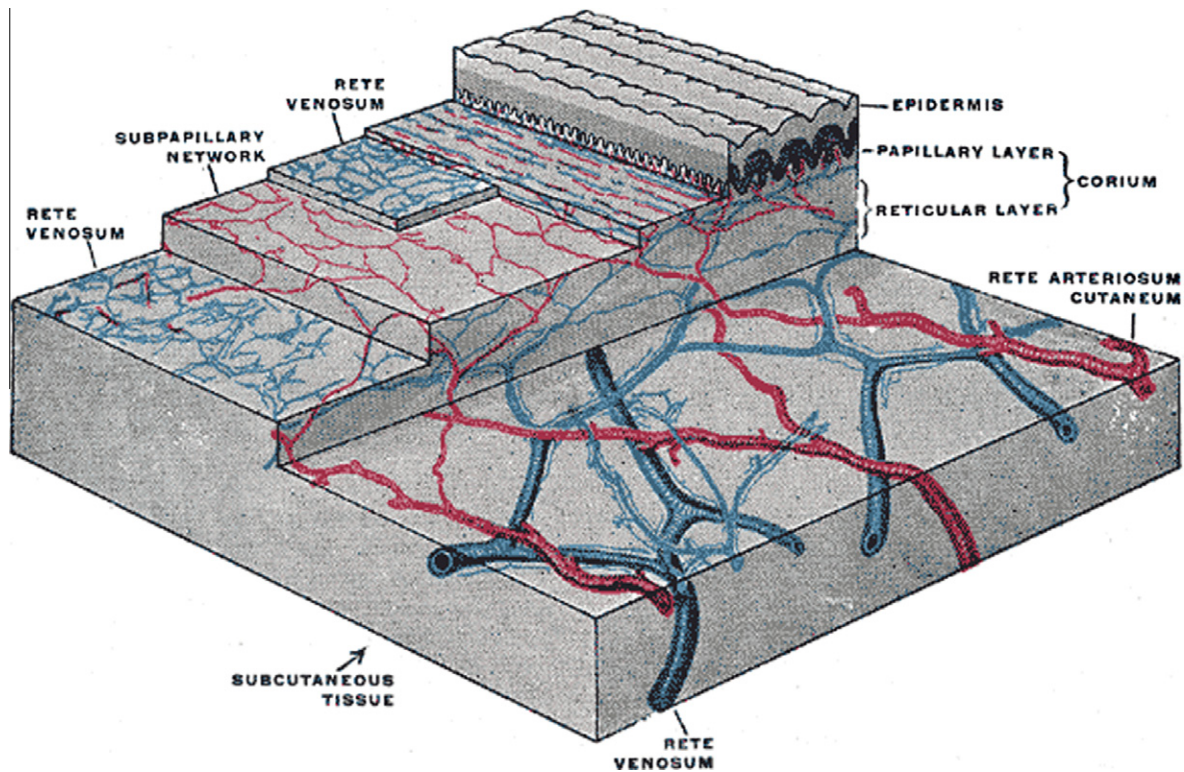
Fig. 1. The distribution of the blood vessels in the skin of the sole of the foot (reproduction of a lithograph plate from Gray's Anatomy). Corium is an alternate term for dermis.

360 ms [12], the T_2 of the dermis has been measured at 28 ms [13], while a T_2^* of 9.8 ms for 90% of the dermis signal has been reported [14]. Recent advances in hardware can help overcome low SNR limitations, such as dedicated surface receiver coil [8], high-temperature superconducting (HTS) receiver surface coils [15,16], high-field spectrometers [17,18] and single-sided NMR probes [19,20]. Recent *in vivo* MR skin studies have made significant progress in increasing the spatial resolution for imaging as well as localized spectroscopy. For imaging, the voxel has gone from $50 \times 150 \times 1000 \ \mu m^3$ at 2 T [12] to $100 \times 130 \times 500 \ \mu m^3$ at 1.5 T [21], and $40 \times 80 \times 900 \ \mu m^3$ [15] with a HTS coil at 1.5 T. Moreover, a voxel of $59 \times 59 \times 59 \ \mu m^3$ with a SNR of 20 has been achieved for *in vivo* microimaging of a mouse with a 12-mm HTS surface coil in a standard clinical 1.5 T whole-body scanner [16]. For spectroscopy, a volume of interest of $0.14 \times 10 \times 10 \ mm^3$ has been successfully used to characterize the biochemical contents of the different skin layers, and empirically correlate relaxation times (T_1 and T_2) to healthy and diseased skin [8].

Diffusion-weighted magnetic resonance (DWMR) protocols have the potential and flexibility to provide quantitative measurements of blood flow without the use of an exogenous contrast agent. DWMR protocols for either spectroscopy or imaging involve the sampling of $\boldsymbol{q}$-space (the Fourier reciprocal space of spin displacements) via the choice of magnetic gradient strengths and directions [22–26]. When combined with an imaging pulse sequence which acquires data in $\boldsymbol{k}$-space (the Fourier reciprocal space of spin locations), DWMR imaging consists of acquiring a series of images, each of which corresponds to one sampling location in $\boldsymbol{q}$-space. In DWMR, a data model for the signal in $\boldsymbol{q}$-space is often used, and the corresponding inverse problem is solved to estimate the model parameters of interest designed to characterize the physical problem under study (e.g., DTI [27], ADTI [28], CHARMED [29], QUAQ [30,31]). Examples include diffusion and perfusion measurements in living tissues [32], and estimation of the vascular volume fraction and mean microflow velocity in canine myocar-

dium [33]. From a pulse sequence programming point-of-view, stimulated-echo pulse sequences [34,33] or single-shot techniques with time-efficient interleaved multi-slice acquisition [18] may be used for DWMR to avoid an excessive drop of signal due to T_2^* relaxation. While apparent diffusion coefficients have been measured at a voxel size of $95 \times 95 \times 1000 \ \mu m^3$ via DWMR in *in vitro* animal skin tissues in a 2 T clinical whole-body MRI system [35], microimaging at 21 T has been performed on hairless rat skin with spatial resolutions down to $19.5 \times 19.5 \times 300 \ \mu m^3$ [17] and $15 \times 15 \times 40 \ \mu m^3$ [18], and several NMR modalities–including DWMR imaging–were evaluated for their usefulness in distinguishing between different skin appendages (stratum corneum, epidermis, reticular dermis, papillary dermis, hair follicle and sebaceous gland).

Besides the experimental noise in the acquired DWMR data, another source of error comes from the way $\boldsymbol{q}$-space is sampled (i.e., the DWMR or $\boldsymbol{q}$-space sampling protocol) and how noise propagates through the inverse problem into the model parameter estimates. Therefore, a key piece of the design of an experiment is to optimize the DWMR protocol (i.e., encoding gradient strengths and directions). Several schemes to pick gradient direction schemes for DTI experiments are reviewed in [36], such as numerically optimized schemes (minimum force, minimum energy, minimum condition number), heuristic schemes (orthogonal encoding) and geometric schemes (icosahedral polyhedra). Jones et al. [37] proposed that in absence of any prior knowledge of the tensor to be estimated (or the imaged structure), gradients can be uniformly distributed in 3-D gradient space by minimizing Coulomb's force (minimum force-MF) between unit charges on a sphere where charges represent the gradient directions. Instead of optimizing the diffusion gradient direction schemes, optimization can also be on the selection of diffusion gradient strength, diffusion pulse duration, diffusion pulse interval and number of diffusion gradient directions, such as in [38]. Brihuega-Moreno et al. [39] used Cramer-Rao lower bounds (CRLB [40,41]) for the optimal selection

of b-values for apparent diffusion coefficient (ADC) measurements by minimizing the CRLB of the ADC with respect to the b-values. Similarly, Cercignani and Alexander [42] applied the CRLB in quantitative magnetization transfer (MT) MRI where they further optimized the MT-MRI acquisition scheme to be robust within the range of MT model parameters observed in the brain. The aforementioned methods assume Gaussian noise model in the definition of CRLB. A more appropriate noise model for the magnitude MR image data used in DTI or ADC measurements is the Rician noise model [43,44] and an application of the CRLB has been demonstrated by Alexander in [38] for the optimization of acquisition parameters using the CHARMED diffusion model [29].

In this paper, we propose an optimization framework for the robust optimal design of DWMR protocols using CRLB for the experimental study of skin microcirculation to complement ongoing hardware advances. Compared to standard optimization [10], the robustness of our DWMR protocols is achieved by incorporating the uncertainty in the *a priori* information, such that the DWMR protocols are optimized against the worst-case scenario.

2. Methods

2.1. DWMR model for skin microcirculation

DWMR protocols via pulsed field gradient MR result in the acquisition of a normalized echo attenuation, $A(\boldsymbol{q}, \Delta) \in \mathbb{C}$, which corresponds to the Fourier transform of the probability density function of the spin displacements [22,45]. $A(\boldsymbol{q}, \Delta)$ is a function of the spatial frequency of the spin displacements, $\boldsymbol{q} := \gamma \boldsymbol{g} \delta / 2\pi \in \mathbb{R}^3$, and Δ, where δ and Δ are the duration of and time between the pulsed field gradients $\boldsymbol{g} \in \mathbb{R}^3$, respectively [22]. Experimentally, $A(\boldsymbol{q}, \Delta)$ is obtained by dividing the measured echo $A^*(\boldsymbol{q}, \Delta)$ with diffusion-encoding gradients turned on ($\boldsymbol{q} \neq \boldsymbol{0}$) by the echo $A_0^* := A^*(\boldsymbol{0}, \Delta)$ obtained with diffusion-encoding gradients turned off ($\boldsymbol{q} = \boldsymbol{0}$) [45]:

$$A(\boldsymbol{q}, \Delta) := \frac{A^*(\boldsymbol{q}, \Delta)}{A_0^*}. \tag{1}$$

In order to obtain a DWMR model for skin microcirculation, an effective physical model for microcirculation in the skin must first be constructed. To do so, the standard advection–diffusion equation that characterizes blood flow in the skin can be volume-averaged and linearized [46]:

$$\frac{\partial C}{\partial t} + \boldsymbol{V} \cdot \nabla C = \boldsymbol{D} \nabla^2 C, \tag{2}$$

which introduces a spatially averaged velocity field, $\boldsymbol{V} := [V_x V_y V_z]^{\mathrm{T}}$, and a symmetric dispersion tensor, $\boldsymbol{D} \in \mathbb{R}^{3 \times 3}$, which reflects on both the advection and diffusion processes, as well as on the geometry, and may be time-dependent [47]. The model parameters, $\boldsymbol{V}$ and $\boldsymbol{D}$, correspond to an effective dispersion model for skin at the chosen voxel scale. It can be shown [48] that the response to an impulse function, $C(x, y, z, 0) = C_0 \delta(x, y, z, 0)$ after a time t is given by

$$C(\mathbf{x}, t) = \frac{C_0}{\sqrt{(4\pi)^3 t^3 (\det \mathbf{D})}} \exp\left[-\frac{(\mathbf{x} - \mathbf{V}t)^{\mathrm{T}} \mathbf{D}^{-1} (\mathbf{x} - \mathbf{V}t)}{4t} \right]. \tag{3}$$

For an impulse initially located at a location $\boldsymbol{x}_0$, $\boldsymbol{x}$ in (3) needs to be replaced by the vector $\boldsymbol{x} - \boldsymbol{x}_0$, which can be thought of as a displacement vector. Then after normalization, (3) provides the probability density function of the spin displacements, which corresponds to the inverse Fourier transform of the DWMR signal $A(\boldsymbol{q}, \Delta)$ [45].

Let us now consider specific DWMR protocols for skin microcirculation. The imaging voxel can be taken such that z is the direction perpendicular to the skin surface (and surface coil). As noted in [11], the blood vessels in the deep horizontal plexus run parallel to the surface of the skin, prompting us to assume that the z-axis is one of the principle axis of the dispersion tensor. As a result, dispersion along the z direction is decoupled from dispersion in the (x, y)-plane, wherein the dispersion along the x- and y-axes is coupled (i.e., in general, $D_{xy} \neq 0$ or the principal axes of the dispersion tensor in the (x, y)-plane are rotated from the x- and y-axes by a non-zero angle). Then, with $\boldsymbol{q} := [q_x, q_y, q_z]^{\mathrm{T}}$, our effective model for $A(\boldsymbol{q}, \Delta)$ is obtained by taking the inverse Fourier transform of (3), leading to

$$A(\mathbf{q}, \Delta) = \exp\left[-4\pi^2 \left(\Delta - \frac{\delta}{3} \right) \left(D_{xx} q_x^2 + D_{yy} q_y^2 + 2 D_{xy} q_x q_y \right) \right]$$
$$\times \exp\left[\mathrm{i} 2\pi \Delta (V_x q_x + V_y q_y) \right]$$
$$\times \exp\left[-4\pi^2 \left(\Delta - \frac{\delta}{3} \right) D_{zz} q_z^2 + \mathrm{i} 2\pi \Delta V_z q_z \right]. \tag{4}$$

This paper focuses on setting up the framework for developing a skin microcirculation model and the robust design optimization of DWMR protocols used for its implementation. Therefore, a simpler model is more appropriate, such that the optimization results can be more readily interpreted and provide a greater insight than if a more complex effective dispersion model were used. However, our framework can accommodate more complex DWMR signal models without any insurmountable difficulties by modifying (4) and using for instance a full dispersion tensor and/or modeling multiple compartments [10], based on a more complex effective dispersion model for skin at the chosen voxel scale.

2.2. Experimental design

On clinical scanners, because of the limited gradient strength capabilities, the values for the duration (δ) and separation (Δ) of the pulsed gradients are quite constrained. The maximum desired value for $\boldsymbol{q}$ is typically achieved by using the maximum allowed gradient strength, which then fixes δ. The value for Δ is then typically chosen in order to minimize the duration of the echo time so as to minimize T_2 relaxation and maximize the SNR. Ideally, one would use a pulse sequence, wherein the diffusion-encoding gradients can be set to zero without modifying the timing of the pulse sequence, and in particular shortening the echo time, such that by taking the ratio $A^*(\mathrm{q}, \Delta)/A_0^*$, the T_2 weighting cancels out. Should such a DWMR pulse sequence not be available on the MRI scanner used and the echo time vary for the data acquired, one would need to take T_2 effects into account as done in [38]. An upper bound for $q := \|\boldsymbol{q}\|$ is imposed to limit the signal attenuation due to diffusion, such that the commonly used b value remains below $b_{max} = 1000 \text{ s mm}^{-2}$, with

$$b := 4\pi^2 q^2 \left(\Delta - \frac{\delta}{3} \right). \tag{5}$$

Moreover, for DWMR, collecting data on a small number of spheres in $\boldsymbol{q}$-space is usually more practical and efficient experimentally [10,49,27]. One reason is that the software on clinical scanners often optimizes the MRI pulse sequence parameters for a given value of q. It is then generally preferable to collect one reference image per value of q, such that when using (1), the signal A_0^* is collected for exactly the same experimental parameters as $A^*(\boldsymbol{q}, \Delta)$, only the diffusion-encoding gradients turned off.

Noise in MR data is modelled as independent Gaussian noise with zero mean in the two quadrature detection channels [43,44]. The sensitivity to noise will determine the required SNR in experimental DWMR data, and thus, ultimately, the voxel size. This numerical analysis of our DWMR model will therefore allow the proper design of MRI protocols and avoid costly trial-and-error repetitions of MRI experiments. The model (4) can be written as $A(\boldsymbol{q}_m, \theta^{\star})$, where $\theta^{\star} \in \mathbb{R}^p$ is the true parameter vector ($p = 7$)

corresponding to the true values for the parameters of our DWMR model for skin microcirculation, namely D_{xx}, D_{yy}, D_{xy}, D_{zz}, V_x, V_y, and V_z. Additionally, the $\boldsymbol{q}$-space sampling protocol is defined as

$$Q_M := \{q_m\}_{m=1}^M, \tag{6}$$

with $M \geqslant p$. Then, since A_0^* is typically quite large compared to $A^*(\boldsymbol{q}, \Delta)$, the Gaussian noise contained in A_0^* is assumed to be negligible compared to that in $A^*(\boldsymbol{q}, \Delta)$, which is consistent with published noise propagation studies (see for example [38,39]), such that the corresponding set of measurements can be written as:

$$\widehat{A}_m := A(q_m, \theta^\star) + e_m, \quad m = 1, \ldots, M, \tag{7}$$

where e_m is a complex-valued white noise random variable with the following properties: its real and imaginary parts are jointly normal and independent, each with zero mean and variance σ^2, such that e_m has variance $2\sigma^2$. The origin of this complex-valued white noise is from the asymptotic normal distribution of the Fourier transform of white noise [50,51]. It may also come from the quantization and electronic noise of the data acquisition system.

The inverse problem then consists in estimating the parameters related to skin microcirculation from our DWMR model (4) given the measurements (7). Using nonlinear least squares (NLS), the parameter estimates $\hat{\theta}_M \in \mathbb{R}^p$ are obtained by minimizing the residual sum of squares:

$$\hat{\theta}_M = \arg \min_{\theta \in \mathbb{R}^p} S_M(\theta), \quad S_M(\theta) := \sum_{m=1}^M \left| \widehat{A}_m - A(q_m, \theta) \right|^2 \tag{8}$$

where $|\cdot|$ denotes the magnitude operator on a complex number. The objective of this manuscript is to numerically find the optimal $\boldsymbol{q}$-space sampling protocol for the DWMR model (4), subject to realistic experimental constraints, such that the uncertainty in the parameter estimates $\hat{\theta}_M$ is minimized.

2.3. Experimental design optimization

The Cramer-Rao Lower Bound (CRLB) provides the minimal achievable estimation error variances by any unbiased estimator [40], i.e., for the given noise model in (7), the estimation error variances resulting from the NLS estimation of the physical parameters of interest according to (8) cannot be smaller than those prescribed by the CRLB. Therefore, it serves as a good criterion to optimize the $\boldsymbol{q}$-space sampling protocol for our DWMR model for skin microcirculation. In particular, by the Cramer-Rao theorem [40], the covariance matrix W of any unbiased estimator $\hat{\theta}_M$ is lower bounded by the CRLB, or the inverse of the Fisher Information Matrix FIM$(\theta^\star, Q_M)$ [41]:

$$W \succeq \mathrm{FIM}(\theta^\star, Q_M)^{-1} = \frac{\sigma^2 \Sigma_{2M}^{-1}(\theta^\star)}{M} =: \mathrm{CRLB} \tag{9}$$

with

$$\Sigma_{2M} := \frac{1}{M} \sum_{m=1}^M \mathrm{Re}\{A'(q_m, \theta^\star)A'(q_m, \Delta, \theta^\star)^*\}, \tag{10}$$

where the positive semi-definiteness of a matrix $A - B$ is denoted by $A - B \succeq 0$ or equivalently $A \succeq B$. Re$\{T\}$ is the (element-wise) real part of matrix T and $A'(q_m, \theta^\star) := \partial A(q_m, \theta) / \partial \theta|_{\theta=\theta^\star}$. Under some regularity conditions [41,52], (9) becomes an equality as $M \to \infty$ (asymptotic normality), such that the right-hand-side of (9) can be used to predict the covariance matrix of the estimates. Hence, this suggests the formulation of an experimental design optimization that aims at decreasing the size of the CRLB in order to improve the quality of the estimation of unknown parameters.

In this work, the problem is to find an optimal configuration of M measurement points, Q_{opt}, such that the size of the confidence

region of the parameter estimates and/or the estimation error variances are reduced. Following the discussion in Section 2.2, we restrict the sampling vectors $\boldsymbol{q}_m$ to be on a single sphere of radius $q < q_{max} := b_{max} / [4\pi^2(\Delta - \delta/3)]$ and centered at the origin, which we denote $\mathscr{S} \subset \mathbb{R}^3$, resulting in $Q_M \in \mathscr{S}^M \subset \mathbb{R}^{3M}$. There are then $(2M + 1)$ variables describing Q_M to optimize: $2M$ spherical angles to define the orientation of the sampling vectors $\boldsymbol{q}_m$ and one variable for their magnitude q. This parameterization is consistent with standard sampling protocols used for DWMR imaging [37].

We consider two optimization criteria: D-optimality [40] in which the determinant of the FIM is maximized, and A-optimality [40,53] in which the trace of the CRLB is minimized. Formally, we solve the following optimization problems:

$$Q_{opt}^\ell := \arg \max_{Q_M \in \mathscr{S}^M} J_\ell(\theta^\star, Q_M) \quad \ell \in \{D, A\}, \tag{11}$$

where J_D is defined for D-optimality,

$$J_D(\theta^\star, Q_M) := \det \left[\frac{1}{\sigma^2} \sum_{m=1}^M \mathrm{Re}\{A'(q_m, \theta^\star)A'(q_m, \theta^\star)^*\} \right], \tag{12}$$

and J_A is defined for A-optimality

$$J_A(\theta^\star, Q_M) := -\mathrm{trace} \left[\frac{\sigma^2 \Sigma_{2M}^{-1}(\theta^\star)}{M} \right]. \tag{13}$$

Remark 1. The minimum of the D-optimal design is invariant to any transformation of the parameter vector θ. However, this measure does not allow to place a hard-bound on each estimation error variance of parameters. Conversely, A-optimality is not invariant to any transformation of θ, and provides a hard-bound on every estimation error variance [53]. In this paper, the units of the model parameters are scaled, so that the terms in $J_A(\theta^\star, Q_M)$ have consistent units [54].

These D- and A-optimal design problems are solved numerically by using a gradient-based method from the optimization toolbox in MatLab (The MathWorks, Natick, MA) for a given $\theta^\star$. In practice, the a priori value θ_0 of $\theta^\star$ may be used instead of the unknown true value for $\theta^\star$ [41]. Alternatively, an a priori estimate of $\theta^\star$ may be available from preliminary data or known range of possible values. The following section deals with optimizing the experimental parameters to take into account such an approximate knowledge of $\theta^\star$.

2.4. Robust experimental design optimization

Consider the model in (7) with $\theta^\star \in \Lambda_\theta$, where the true parameter vector $\theta^\star$ is contained in an uncertain parameter set Λ_θ, i.e., Λ_θ is an available a priori knowledge. Then our robust experimental design problem with respect to the uncertain parameter set can be formulated as follows [53]: find Q_M in order to maximize the worst case of $J_\ell(\theta^\star, Q_M)$, given in (11)–(13), i.e., solve the following robust optimization problems:

$$Q_{rob}^\ell = \arg \max_{Q_M \in \mathscr{S}^M} \min_{\theta \in \Lambda_\theta} J_\ell(\theta, Q_M) \quad \ell \in \{D, A\}. \tag{14}$$

In order to deal with the optimization problems in (14), let us introduce the uncertain parameter set Λ_θ containing the true parameter vector value $\theta^\star$ more specifically as a Cartesian product of intervals

$$\Lambda_\theta := \Pi_{i=1}^p [\theta_i^L, \theta_i^H] = [\theta_1^L, \theta_1^H] \times [\theta_2^L, \theta_2^H] \times \cdots \times [\theta_p^L, \theta_p^H], \tag{15}$$

where θ_i^L and θ_i^H are the lower and upper bounds for each model parameter θ_i, respectively. The robust optimization problems described by (14) can be solved by using a trajectory-following gradient algorithm for max–min optimization [55]. Supposing that the max–min solution exists for (14) and that the limits on the decision

variable are suitable such that it is unique, the trajectory then converges to the unique stationary solution for (14), i.e., $\lim_{t\to\infty}\theta(t) = \theta^*$, and $\lim_{t\to\infty}Q_M(t) = Q_M^*$ [55]. However, in general, the solution can be non-unique and can be located at the boundary of $\Lambda_\theta \times \mathscr{S}^M$.

To avoid local minima and achieve a fast convergence rate for the trajectory $\{[\theta(t), Q_M(t)] \in \Lambda_\theta \times \mathscr{S}^M, t \in \mathbb{N}\}$, where t is a fictitious discrete time variable, the following iterative algorithm is implemented. At each step of the algorithm, the change from t to $t + 1$ along each coordinate in $\Lambda_\theta \times \mathscr{S}^M$ is done by introducing:

$$\theta^{\min}(t) := \arg\min_{\theta \in \Lambda_\theta} J_\ell(\theta, Q_M(t)), \tag{16}$$

which is solved by sampling Λ_θ at discrete locations, computing J_ℓ at these locations for the current configuration Q, and then picking the value for $\theta^{\min}$ that minimizes the sampled values for J_ℓ. Then, at the next iteration,

$$\theta(t + 1) = \theta^{\min}(t), \tag{17}$$

and, with $\epsilon > 0$ is a small positive number,

$$q_m(t + 1) = q_m(t) + \epsilon \frac{\partial J_\ell}{\partial q_m}(\theta^{\min}(t), Q_M(t)). \tag{18}$$

Thus, $\theta^{\min}$ satisfies that $\partial J_\ell(\theta^{\min}, Q_M)/\partial \theta_i \approx 0$ and $\partial^2 J_\ell(\theta^{\min}, Q_M)/\partial \theta_i^2 > 0$, or that $\theta_i = \theta_i^L$ or θ_i^H, for all $i = 1, \ldots, p$. To counteract the effect of the discrete sampling, when $\theta_i \neq \theta_i^L$ or θ_i^H, a better estimate for the location of $\theta_i^{\min}$ is obtained by parabolic fitting. The algorithm (17),(18) stops when $\theta_i(t + 1) - \theta_i(t) \approx 0$ for $i = 1, \ldots, p$ and $q_m(t + 1) - q_m(t) \approx 0$ for $m = 1, \ldots, M$ for all future time; we then apply a gradient search algorithm starting from the states obtained from the previous step.

Our numerical results reveal that solving the robust optimization using our proposed combined algorithm represented by (17) and (18) is much more efficient in terms of computational time and local critical points than using a trajectory-following gradient algorithm [55] alone.

3. Results

The NLS estimator for our DWMR model (4) to quantify skin microcirculation is evaluated by analysing the covariance matrices from the NLS estimation using Monte-Carlo (MC) simulations with K realizations and a noise level $\sigma = 5\%$. The performance with other noise levels can be obtained from (9), which indicates that for a given q-space sampling protocol the standard deviations of the NLS estimates scale linearly with the noise level σ. The parameter estimation is done using the Levenberg–Marquardt algorithm [56] with an initial guess equal to a vector with a 10% deviation from the true parameter $\theta^\star$. The number K of MC realizations is chosen such that the predicted standard deviations converge towards their predicted values, which is achieved for $K = 20\,000$. A set of realistic experimental parameters is chosen (see Table 1): $\Delta = 3$ s, $\delta = 0.03$ s, and the values of the coefficients of the dispersion tensor are chosen by selecting three eigenvalues (here, $\{3.0, 2.2, 2.5\} \times 10^{-3}$ mm^2 s^{-1}) corresponding to the x-, y- and z-axis and performing a rotation of angle $\alpha_0 = \pi/3$ about the z-axis.

3.1. Performance of our D- and A-optimal experimental protocols

Three sets of q-space sampling protocols ($M = 12$) identified by sets of locations on one sphere are compared: our D-optimal (Q_{opt}^D) and A-optimal (Q_{opt}^A) q-space sampling protocols obtained from (11)–(13), and a conventional sampling protocol denoted by Q_P based on Papadakis' scheme 12 [49], which was used experimentally in [33] for instance. For Q_P, the gradient magnitude defining the sphere was optimized. For our DWMR model (4) and the chosen $\theta^\star$, the optimal radius of the sphere for both the D-optimal and

Table 1
Comparison of the NLS estimates obtained with conventional (Q_P), D-optimal (Q_{opt}^D) and A-optimal (Q_{opt}^A) q-space sampling protocols containing $M = 12$ sampling locations for $\sigma = 5\%$ noise. The computed values result from MC simulations ($K = 20\,000$). The values for D_{xx}, D_{yy}, D_{zz}, D_{xy}, and D_{surr} are expressed in 10^{-3} mm^2 s^{-1}. The values for V_x, V_y and V_z are expressed in mm s^{-1}.

	$\theta^\star$	Mean values		
		Q_P	Q_{opt}^D	Q_{opt}^A
D_{xx}	2.400	2.402	2.402	2.402
D_{yy}	2.800	2.801	2.799	2.804
D_{zz}	2.500	2.499	2.501	2.501
D_{xy}	−0.346	−0.346	−0.347	−0.349
V_x	0.300	0.299	0.300	0.300
V_y	0.400	0.400	0.400	0.400
V_z	0.100	0.100	0.100	0.100

A-optimal q-space sampling protocols (Q_{opt}^D and Q_{opt}^A, respectively) was determined to be $q \approx 17.9$ mm^{-1}, corresponding to $b \approx 342$ s mm^{-2}, while for the conventional sampling protocol (Q_P) was determined to be $q \approx 17.1$ mm^{-1}, corresponding to $b \approx 312$ s mm^{-2}.

The unit gradient directions corresponding to the D-optimal, A-optimal and conventional q-space sampling protocols are shown in Figs. 2 and 3. It is quite apparent that both optimal sampling protocols have the particularity of having one sampling location at each pole and ten sampling locations around the equator. Given the symmetry with respect to the (x, y)-plane (i.e., the plane of the equator) of the chosen model, it was to be expected. This observation provides an intrinsic verification of our optimization procedure.

The three q-space sampling protocols are compared via Tables 1 and 2, which report on the mean values and standard deviations, respectively, of the NLS estimates as well as the analytical predictions of the latter using the asymptotic normality of the NLS estimates [41,52]. Table 1 reveals that the NLS estimator is unbiased, since the mean values of the NLS estimates of the model parameters match $\theta^\star$. Moreover, Table 2 demonstrates that the covariance matrix of the NLS estimates agrees very well with the CRLB. Therefore, the variances of the NLS estimates can be easily predicted using (9). The standard deviations of the NLS estimates resulting
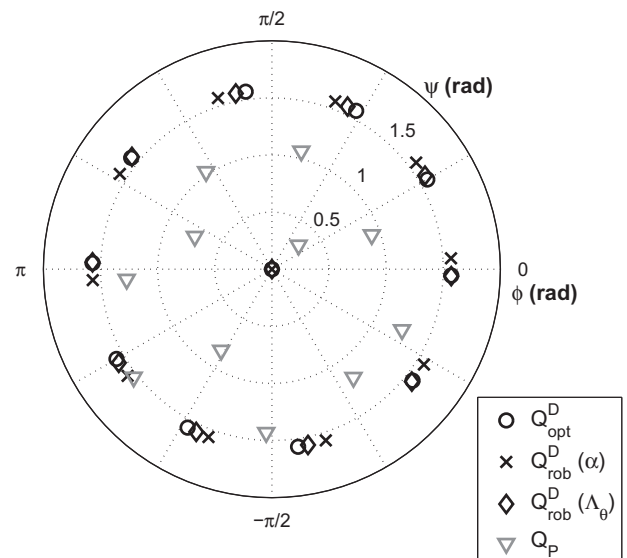

Fig. 2. Polar plot of the unit gradient directions used in the pure D-optimal (Q_{opt}^D), robust D-optimal ($Q_{rob}^D(\alpha)$ and $Q_{rob}^D(\Lambda_\theta)$ corresponding to the cases when $(\alpha - \alpha_0) \in [-\pi/9, \pi/9]$ and $\theta^\star \in \Lambda_\theta$, respectively) and conventional (Q_P) q-space sampling protocols.
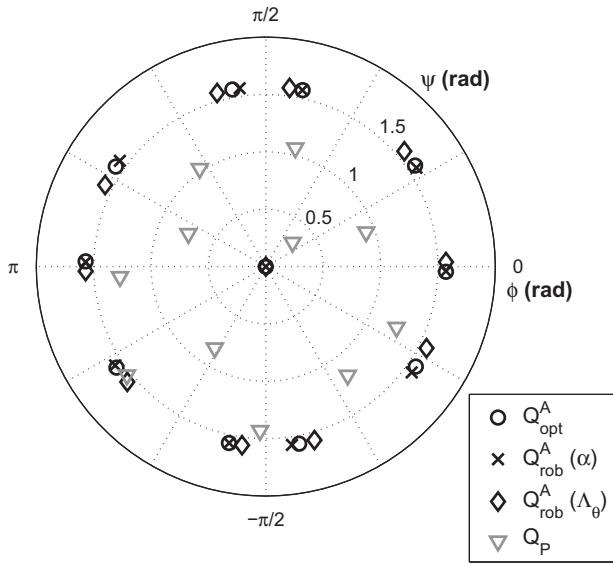
Fig. 3. Polar plot of the unit gradient directions used in the pure A-optimal (Q_{opt}^A), robust A-optimal ($Q_{rob}^A(\alpha)$ and $Q_{rob}^A(\Lambda_\theta)$ corresponding to the cases when $(\alpha - \alpha_0) \in [-\pi/9, \pi/9]$ and $\theta^\star \in \Lambda_\theta$, respectively) and conventional (Q_P) q-space sampling protocols.

Table 2
Comparison of the standard deviations obtained with conventional (Q_P), D-optimal (Q_{opt}^D) and A-optimal (Q_{opt}^A) q-space sampling protocols containing $M = 12$ sampling locations for $\sigma = 5\%$ noise. The computed values result from MC simulations ($K = 20000$). The units used are the same as the ones used for Table 1.

	$\theta^\star$	Standard deviations for $\sigma = 5\%$					
		Q_P		Q_{opt}^D		Q_{opt}^A	
		MC	Predicted	MC	Predicted	MC	Predicted
D_{xx}	2.400	0.246	0.244	0.183	0.185	0.177	0.179
D_{yy}	2.800	0.264	0.265	0.213	0.212	0.195	0.193
D_{zz}	2.500	0.249	0.249	0.248	0.248	0.244	0.244
D_{xy}	−0.346	0.200	0.200	0.165	0.164	0.175	0.175
V_x	0.300	0.017	0.017	0.015	0.015	0.015	0.015
V_y	0.400	0.018	0.018	0.016	0.016	0.016	0.016
V_z	0.100	0.017	0.017	0.024	0.024	0.024	0.024

from Q_{opt}^D and Q_{opt}^A are smaller than those from Q_P with improvements up to 33%, except for V_z, for which the standard deviation increases slightly.

3.2. Performance of our robust D-optimal and A-optimal sampling protocols

Robust optimization of the q-space sampling protocol using D- and A-optimality is conducted following (11)–(17). To that end, an uncertainty set must be defined (e.g., an interval Λ_θ defined as a product of uncertainty intervals for each of the model parameters as in (15) in Section 2.4). In a first illustrative example, only one physical parameter is varied within an uncertainty set, such that the optimization function can be plotted vs. this parameter. To preserve some physical meaning as well as generality, we chose to define our uncertainty as a function of the rotation angle α about the z-axis of our physical model, namely $\alpha \in [\alpha_0 - \pi/9, \alpha_0 + \pi/9]$, such that five of our model parameters (i.e., D_{xx}, D_{xy}, D_{yy}, V_x and V_y) are allowed to vary, while the other two (D_{zz} and V_z) are constant. The model parameters used for the pure optimization correspond to $\alpha = \alpha_0 = \pi/3$.

The unit gradient directions corresponding to the resulting robust D-optimal and A-optimal q-space sampling protocols are

plotted and compared to the conventional, pure D-optimal and A-optimal q-space sampling protocols in Figs. 2 and 3, respectively, while $q \approx 17.9 \text{ mm}^{-1}$ as for the pure optimal protocols. One observes a slight shift of the positions of the sampling locations of the robust optimal sampling protocols ($Q_{rob}^D(\alpha)$ and $Q_{rob}^A(\alpha)$, respectively) with respect to those of the pure optimal protocols (Q_{opt}^D and Q_{opt}^A, respectively) around the equator, in order to reduce the uncertainty of the worst-case estimation within the range $\alpha \in [\alpha_0 - \pi/9, \alpha_0 + \pi/9]$.

In order to assess the performance of robust optimization, Table 3 reports the worst values of the normalized determinant of the FIM, J_D/J_D^0, and the normalized trace of the CRLB, $-J_A/J_A^0$ obtained when α spans the interval $[\alpha_0 - \pi/9, \alpha_0 + \pi/9]$ for the D-optimal (Q_{opt}^D), robust D-optimal (Q_{rob}^D), A-optimal (Q_{opt}^A), and robust A-optimal (Q_{rob}^A) q-space sampling protocols. Additionally, MC simulations are run to compute the standard deviations (see Table 4) for the worst cases defined in Table 3 for each of the optimized sampling protocols. Moreover, J_D/J_D^0 is plotted as a function of the rotation angle α in Fig. 4, while Fig. 5 illustrates the variation of the normalized trace of the CRLB, $-J_A/J_A^0$, as a function of α. In both cases, the figures at the top show the optimization function for the whole range of $\alpha \in [0, \pi]$, while the figures at the bottom provide a zoom on the robust optimization region, $\alpha \in [\alpha_0 - \pi/9, \alpha_0 + \pi/9]$, for the pure (subscript "opt") and robust (subscript "rob") optimization sampling protocols obtained with both D- and A-optimality. The solid lines represent the results for pure optimization, while the dashed lines are for robust optimization. The results for pure and robust D-optimal protocols are in black, the ones for pure and robust A-optimal protocols are in dark gray, and the ones for the conventional sampling protocol are in light gray. J_ℓ^0 ($\ell \in \{D, A\}$) are chosen such that $J_\ell/J_\ell^0 = 1$ when $\alpha = \alpha_0$. For D-optimality, J_D/J_D^0 is maximum, while $-J_A/J_A^0$ is minimum for A-optimality.

It is noteworthy to compare the performance of the A-optimal sampling protocols in terms of the normalized determinant of the FIM (i.e., the optimization function used for D-optimality) with that of the D-optimal sampling protocols in Fig. 4. Similarly, Fig. 5 allows for comparison of the performance of the D-optimal sampling protocols in terms of the normalized trace of the CRLB (i.e., the optimization function used for A-optimality) with that of the A-optimal sampling protocols. Clearly, the A-optimal sampling protocols do not perform as well as the D-optimal sampling protocols in terms of J_D/J_D^0, and vice versa in terms of $-J_A/J_A^0$. Nonetheless, both D- and A-optimal sampling protocols significantly outperform the conventional sampling protocol $Q_P : J_D/J_D^0 > 0.89$ for our optimized sampling protocols compared to $J_D/J_D^0 < 0.34$ for Q_P, and $-J_A/J_A^0 < 1.025$ vs. >1.27 for Q_P. Moreover, robust optimization is effective in improving the worst-case scenario compared to the pure optimization. As shown in Figs. 4 and 5, if α takes the nominal value α_0, then the pure optimization achieves the best performance. However, the robust optimization always produces the best worst-case performance over the uncertain parameter set $\alpha \in [\alpha_0 - \pi/9, \alpha_0 + \pi/9]$.

A second illustrative example is used for verification of the trends observed in the first example. An uncertainty interval Λ_θ is defined according to (15) as the product of the intervals spanned by each of the model parameters as the angle α is varied from $\alpha_0 - \pi/9$ to $\alpha_0 + \pi/9$, and new robust optimal q-space sampling protocols are computed. The unit gradient directions corresponding to these new robust D-optimal and A-optimal q-space sampling protocols are plotted and compared to the previously mentioned q-space sampling protocols in Figs. 2 and 3, respectively, while $q \approx 17.9 \text{ mm}^{-1}$ as for the previous optimal protocols. One observes a slight shift of the positions of the sampling locations of the robust optimal sampling protocols ($Q_{rob}^D(\Lambda_\theta)$ and $Q_{rob}^A(\Lambda_\theta)$, respectively) with respect to those of the pure optimal protocols (Q_{opt}^D and

Table 3
Comparison of the normalized determinant of the FIM, J_D/J_D^0, and the normalized trace of the CRLB, $-J_A/J_A^0$ for the D-optimal (Q_{opt}^D), robust D-optimal (Q_{rob}^D), A-optimal (Q_{opt}^A), and robust A-optimal (Q_{rob}^A) q-space sampling protocols at their respective worst cases with $(\alpha - \alpha_0) \in [-\pi/9, \pi/9]$.

	Optimization functions for the worst cases ($\alpha - \alpha_0 \in [-\pi/9, \pi/9]$)							
	Q_{opt}^D		Q_{rob}^D		Q_{opt}^A		Q_{rob}^A	
J_D/J_D^0	0.9905	–	0.9915	–	0.9015	–	0.8937	–
$-J_A/J_A^0$	–	1.0247	–	1.0229	–	1.0023	–	1.0018

Table 4
Comparison of the standard deviations obtained with the D-optimal (Q_{opt}^D), robust D-optimal (Q_{rob}^D), A-optimal (Q_{opt}^A), and robust A-optimal (Q_{rob}^A) q-space sampling protocols at their respective worst cases (within $\alpha \in [\alpha_0 - \pi/9, \alpha_0 + \pi/9]$). The MC parameters and units used are the same as the ones used for Table 1. Table 3 lists the values of the optimization functions corresponding to the worst cases.

|	Standard deviations for the worst cases							
	Q_{opt}^D		Q_{rob}^D		Q_{opt}^A		Q_{rob}^A	
	MC	Predicted	MC	Predicted	MC	Predicted	MC	Predicted
D_{xx}	0.178	0.178	0.179	0.180	0.172	0.172	0.172	0.173
D_{yy}	0.220	0.220	0.219	0.218	0.203	0.202	0.199	0.200
D_{zz}	0.249	0.248	0.247	0.248	0.243	0.244	0.244	0.244
D_{xy}	0.163	0.162	0.162	0.161	0.174	0.173	0.174	0.174
V_x	0.014	0.014	0.014	0.014	0.015	0.015	0.015	0.015
V_y	0.017	0.017	0.017	0.017	0.017	0.017	0.017	0.017
V_z	0.024	0.024	0.024	0.024	0.024	0.024	0.025	0.024
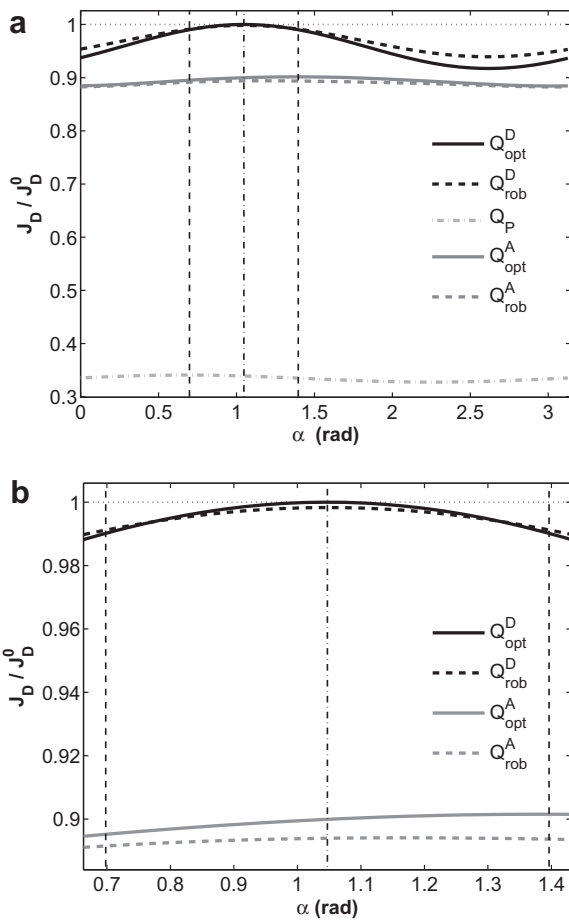
Fig. 4. Plot of the normalized determinant of the FIM, J_D/J_D^0 as a function of the rotation angle α about the z-axis of the physical model for the pure and robust D-optimal (Q_{opt}^D and Q_{rob}^D, respectively) and A-optimal (Q_{opt}^A and Q_{rob}^A, respectively) q-space sampling protocols using $\alpha = \alpha_0 = \pi/3$ and for the conventional sampling protocol Q_P: (a) $\alpha \in [0, \pi]$; (b) larger view for $\alpha \in [\alpha_0 - \pi/9, \alpha_0 + \pi/9]$. For D-optimality, J_D/J_D^0 is maximized and equal to 1 at $\alpha = \alpha_0$.
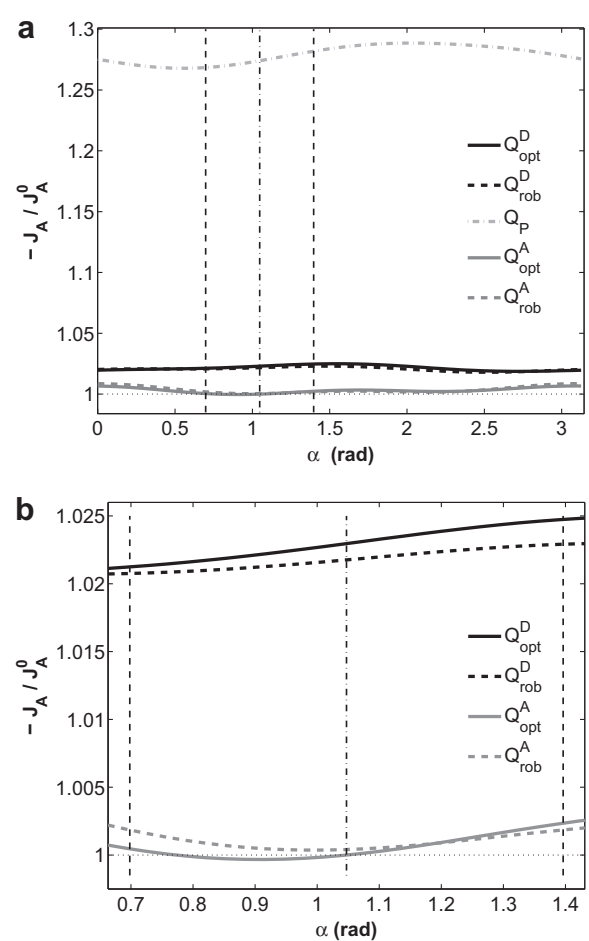
Fig. 5. Plot of the normalized trace of the CRLB, $-J_A/J_A^0$ as a function of α for the pure and robust D-optimal (Q_{opt}^D and Q_{rob}^D, respectively) and A-optimal (Q_{opt}^A and Q_{rob}^A, respectively) q-space sampling protocols using $\alpha_0 = \pi/3$ and for the conventional sampling protocol Q_P: (a) $\alpha \in [0, \pi]$; (b) larger view for $\alpha \in [\alpha_0 - \pi/9, \alpha_0 + \pi/9]$. For A-optimality, $-J_A/J_A^0$ is minimized and equal to 1 at $\alpha = \alpha_0$.

Table 5

Comparison of the normalized determinant of the FIM, J_D/J_D^0, and the normalized trace of the CRLB, $-J_A/J_A^0$ for the D-optimal (Q_{opt}^D), robust D-optimal (Q_{rob}^D), A-optimal (Q_{opt}^A), and robust A-optimal (Q_{rob}^A) $\boldsymbol{q}$-space sampling protocols at their respective worst cases with $\theta^\star \in \Lambda_\theta$.

	Optimization functions for the worst cases ($\theta^\star \in \Lambda_\theta$)							
	Q_{opt}^D		Q_{rob}^D		Q_{opt}^A		Q_{rob}^A	
J_D/J_D^0	0.013	–	0.017	–	0.008	–	0.02	–
$-J_A/J_A^0$	–	2.011	–	2.053	–	2.136	–	1.9509

Q_{opt}^A, respectively) and the previous robust optimal protocols ($Q_{rob}^D(\alpha)$ and $Q_{rob}^A(\alpha)$, respectively) around the equator, in order to reduce the uncertainty of the worst-case estimation within the new range $\theta^\star \in \Lambda_\theta$.

As for the previous example, the worst values of the normalized determinant of the FIM and the normalized trace of the CRLB for our previous pure D- and A-optimal $\boldsymbol{q}$-space sampling protocols and our new robust D- and A-optimal $\boldsymbol{q}$-space sampling protocols are tabulated in Table 5. These results confirm the success of our algorithm in that the uncertainty in the parameter estimates in the worst cases for our robust protocols is lower as per our optimization functions than that for our pure optimal protocols. The only difference with our previous example is that the optimization functions for the worst cases here are farther from optimality (unity), which can be explained by the larger uncertainty set Λ_θ (a 5-D hypervolume vs. a 1-D segment). MC simulations were also conducted with an outcome in complete accordance with that of our previous example.

3.3. Discussion

The NLS estimator for our DWMR model (4) is not biased, unlike typical estimation problems encountered in MRI, wherein signal amplitudes as opposed to complex signals are processed, thereby resulting in a noise in the signal amplitude actually following a Rician distribution with non-zero mean [43,44,57] instead of a Gaussian distribution. In particular, data models used for DWMR often use the *amplitude* of the DWMR data while neglecting the phase of the data, such that the corresponding NLS estimators are biased. However, other than recently in [38], studies on model analysis and optimization [49,37,58,28] typically assume Gaussian noise for simplicity because Rician noise is only available as an integral formula, which does not lends itself to straightforward analytical or numerical investigations, such that the resulting $\boldsymbol{q}$-space sampling protocols do not exactly reproduce the designed outcome. By taking into account both the amplitude and the phase of the signal, i.e., a complex signal with superimposed complex Gaussian noise, our analysis obviates these problems and the use of a CRLB with Gaussian noise is more appropriate. While robust optimization has been implemented for MT-MRI in [42], wherein a CRLB with Gaussian noise is used for magnitude MR images, we use robust optimization in the context of designing DWMR protocols, thereby directly incorporating the uncertainty in the *a priori* knowledge of our model parameters, in conjunction with a physical model of the complex MR signal for skin microcirculation, thereby allowing the use of a CRLB with Gaussian noise.

Figs. 4 and 5 clearly demonstrate the superior performance of our D-optimal and A-optimal sampling protocols compared to a conventional protocol. While the differences between pure and robust optimization results are not overwhelming for our particular DWMR model and the specific model parameters chosen here, the example provided in Section 3.2 adequately illustrates the difference between the two approaches and the importance of robust optimization. Since the numerical method used to achieve robust optimization outlined in Section 2.4 does not require much more computational time as that used for pure optimization, one should

always attempt to follow this approach provided an uncertain parameter set (i.e., model parameters with known bounds). It is noted that, in practice, as long as the model is derived from physical principles or preliminary data is available, such uncertain parameter sets can be easily determined. In doing so, it is recommended to obtain the smallest uncertainty set for the robust optimization in order to achieve its worst-case performance at a level that is comparable to the one achieved by the pure optimization with the true parameter values. This can be easily seen from the fact that, if the true parameter values $\theta^\star$ are given such that $\theta^\star \in \Lambda_1 \subset \Lambda_2$ (i.e., Λ_1 represent a smaller uncertainty set for the true parameters compared to Λ_2), then $J_1 = \max_Q \min_{\theta \in \Lambda_1} J(\theta, Q) \geqslant J_2 = \max_Q \min_{\theta \in \Lambda_2} J(\theta, Q)$ (i.e., the robust DWMR protocol based on the smaller uncertainty set Λ_1 can only perform better than the robust DWMR protocol based on the larger uncertainty set Λ_2).

4. Conclusions

A general experimental design framework allowing the investigation of skin microcirculation by DWMR is proposed based on a physical model of the DWMR complex signal for skin microcirculation. Starting from an effective dispersion model of skin resulting from a linearized volume-averaged advection-diffusion equation, an expression for the complex DWMR signal is obtained, and depends on experimental parameters as well as model parameters which represent physical quantities of interest. Then, the $\boldsymbol{q}$-space sampling schemes used to obtain the DWMR data are optimized based on D- and A-optimality in order to counteract the inherently low SNR caused by the short relaxation times of skin tissues and reduce the uncertainty in the NLS parameter estimates. A robust optimization method is also presented in order to further optimize the $\boldsymbol{q}$-space sampling protocols when *a priori* knowledge of an uncertainty set for the model parameters is available. Our models and our optimized vs. conventional $\boldsymbol{q}$-space sampling schemes are validated via MC simulations. Our numerical results reveal the vast improvement in the model parameter estimation by using our optimal sampling schemes compared to a conventional sampling scheme. Moreover, our robust optimal sampling schemes achieve the goal of minimizing the worst case of the uncertainty in parameter estimation within an uncertainty set for the model parameters, which is of crucial interest when model parameters can take any value within a prescribed set. This manuscript is thus meant as a tool to design quantitative DWMR protocols for skin microcirculation studies (e.g., to investigate chronic venous insufficiency or diabetes) and as a complement to ongoing hardware advances. The future of this work is to experimentally implement our modeling and sampling protocols in combination with using high-end hardware and conduct *in vivo* skin microcirculation studies.

References

[1] A. Humeau, W. Steenbergen, H. Nilsson, T. Strömberg, Laser Doppler perfusion monitoring and imaging: novel approaches, Med. Biol. Eng. Comput. 45 (2007) 421–435.
[2] W. Duran, P.J. Pappas, G.W. Schmid-Schönbein, Microcirculatory inflammation in chronic venous insufficiency: current status and future directions, Microcirculation 7 (2000) S49–S58.

[3] R.L. Greenman, S. Panasyuk, X. Wang, T.E. Lyons, T. Dinh, L. Longoria, J.M. Giurini, J. Freeman, L. Khaodhiar, A. Veves, Early changes in the skin microcirculation and muscle metabolism of the diabetic foot, Lancet 366 (2005) 1711–1717.

[4] L.J. Gould, M. Leong, J. Sonstein, S. Wilson, Optimization and validation of an ischemic wound model, Wound Rep. Reg. 13 (2005) 576–582.

[5] M. Larsson, T. Strömberg, Toward a velocity-resolved microvascular blood flow measure by decomposition of the laser Doppler spectrum, J. Biomed. Opt. 11 (2006) 014024.

[6] J. Welzel, Optical coherence tomography in dermatology: a review, Skin Res. Technol. 7 (2001) 1–9.

[7] P.J. Caspers, G.W. Lucassen, G.J. Puppels, Combined in vivo confocal Raman spectroscopy and confocal microscopy of human skin, Biophys. J. 85 (2003) 572–580.

[8] B. Querleux, Magnetic resonance imaging and spectroscopy of skin and subcutis, J. Cosmet. Dermatol. 3 (2004) 156–161.

[9] C. Suihko, L.D. Swindle, S.G. Thomas, J. Serup, Fluorescence fibre–optic confocal microscopy of skin in vivo: microscope and fluorophores, Skin Res. Technol. 11 (2005) 254–267.

[10] G. Cordier, J. Choi, L.G. Raguin, Evaluation of three inverse problem models to quantify skin microcirculation using diffusion-weighted MRI, J. Phys.: Conf. Series 135 (2008) 012031.

[11] C.I. Wright, C.I. Kroner, R. Draijer, Non-invasive methods and stimuli for evaluating the skin's microcirculation, J. Pharmacol. Toxicol. 54 (2006) 1–25.

[12] F. Mirrashed, J.C. Sharp, In vivo morphological characterisation of skin by MRI micro-imaging methods, Skin Res. Technol. 10 (2004) 149–160.

[13] S. Richard, B. Querleux, J. Bittoun, I. Idly-Peretti, O. Jolivet, E. Cermakova, J.L. Lévêque, In vivo proton relaxation times analysis of the skin layers by magnetic resonance imaging, J. Invest. Dermatol. 97 (1991) 120–125.

[14] H.K. Song, F.W. Wehrli, J. Ma, In vivo MR microscopy of the human skin, MRM 37 (1997) 185–191.

[15] J. Ginefri, L. Darrasse, P. Crozat, High-temperature superconducting surface coil for in vivo microimaging of the human skin, MRM 45 (2001) 376–382.

[16] M. Poirier-Quinot, J. Ginefri, O. Girard, P. Robert, L. Darrasse, Performance of a miniature high-temperature superconducting (HTS) surface coil for in vivo microimaging of the mouse in a standard 1.5 T clinical whole-body scanner, MRM 60 (2008) 917–927.

[17] R. Sharma, S. Fulzele, K. Shetty, M. Sachdeva, B.R. Locke, 21 Tesla micro-MRI of rat skin, in: Proc. Int. Soc. Magn. Reson. Med., 2006, p. 2001.

[18] R. Sharma, Microimaging of hairless rat skin by magnetic resonance at 900 MHz, Magn. Reson. Imaging 27 (2009) 240–255.

[19] J. Perlo, F. Casanova, B. Blümich, Profiles with microscopic resolution by single-sided nmr, JMR 176 (2005) 64–70.

[20] B. Blümich, J. Perlo, F. Casanova, Mobile single-sided nmr, Prog. Nucl. Magn. Reson. Spectrosc. 52 (2008) 197–269.

[21] J. Weis, G. Aström, B. Vinnars, A. Wanders, H. Ahlström, Chemical-shift micro-imaging of subcutaneous lesions, Magn. Reson. Mater. Phys. 18 (2005) 59–62.

[22] E.O. Stejskal, Use of spin echoes in a pulsed magnetic-field gradient to study anisotropic, restricted diffusion and flow, J. Chem. Phys. 43 (1965) 3597–3603.

[23] P.T. Callaghan, Y. Xia, Velocity and diffusion imaging in dynamic NMR microscopy, J. Magn. Reson. 91 (1991) 326–352.

[24] P.J. Basser, J. Matiello, D. Le Bihan, MR diffusion tensor spectroscopy and imaging, Biophys. J. 66 (1994) 259–267.

[25] D. Le Bihan, Diffusion and Perfusion Magnetic Resonance Imaging, Raven Press, New York, 1995.

[26] P.J. Basser, Relationships between diffusion tensor and q-space MRI, Magn. Reson. Med. 47 (2002) 392–397.

[27] P.J. Basser, D.K. Jones, Diffusion-tensor MRI: theory, experimental design and data analysis – a technical review, NMR Biomed. 15 (2002) 456–467.

[28] S. Majumdar, D.C. Zhu, S.S. Udpa, L.G. Raguin, Optimization of diffusion encoding gradients in axisymmetric diffusion tensor imaging using a priori structure information, in: Proc. Int. Soc. Magn. Reson. Med., 2009, p. 3513.

[29] Y. Assaf, R.Z. Freidlin, G.K. Rohde, P.J. Basser, New modeling and experimental framework to characterize hindered and restricted water diffusion in brain white matter, Magn. Reson. Med. 52 (2004) 965–978.

[30] L.G. Raguin, D. Hernando, D.C. Karampinos, L. Ciobanu, B.P. Sutton, Z.-P. Liang, J.G. Georgiadis, Quantitative analysis of q-space MRI data, in: J. Hozman, P. Kneppo (Eds.), IFMBE Proc. 3rd European Medical and Biological Engineering Conference, vol. 11, 2005.

[31] L.G. Raguin, D. Hernando, D.C. Karampinos, L. Ciobanu, B.P. Sutton, Z.-P. Liang, J.G. Georgiadis, Quantitative analysis of q-space MRI data: theoretical and experimental validation, in: Proc. Int. Soc. Magn. Reson. Med., 2006, p. 2729.

[32] D. Le Bihan, E. Breton, D. Lallemand, M.L. Aubin, J. Vignaud, M. Laval-Jeantet, Separation of diffusion and perfusion in intra voxel incoherent motion MR imaging, Radiology 168 (1988) 497–505.

[33] V. Callot, E. Bennett, U.K.M. Decking, R.S. Balaban, H. Wen, In vivo study of microcirculation in canine myocardium using the IVIM method, Magn. Reson. Med. 50 (2003) 531–540.

[34] J.E. Tanner, Use of the stimulated echo in NMR diffusion studies, J. Chem. Phys. 52 (1970) 2523–2526.

[35] D.H. Lee, J.I. Kim, H.K. Lee, Investigation of biochemical changes in skin layers by NMR microscopy, Skin Res. Technol. 4 (1998) 142–146.

[36] K.M. Hasan, D.L. Parker, A.L. Alexander, Comparison of gradient encoding schemes for diffusion-tensor MRI, J. Magn. Reson. Imaging 13 (2001) 769–780.

[37] D.K. Jones, M.A. Horsfield, A. Simmons, Optimal strategies for measuring diffusion in anisotropic systems by magnetic resonance imaging, Magn. Reson. Med. 42 (1999) 515–525.

[38] D.C. Alexander, A general framework for experiment design in diffusion MRI and its application in measuring direct tissue-microstructure features, Magn. Reson. Med. 60 (2008) 439–448.

[39] O. Brihuega-Moreno, F.P. Heese, L.D. Hall, Optimization of diffusion measurements using Cramer-Rao lower bound theory and its application to articular cartilage, Magn. Reson. Med. 50 (2003) 1069–1076.

[40] A.F. Emery, A.V. Nenarokomov, Optimal experiment design, Meas. Sci. Technol. 9 (1998) 864–876.

[41] R. Nagamune, J. Choi, Parameter reduction of nonlinear least-squares estimates via singular value decomposition, in: Proc. 17th Int. Fed. Autom. Control (IFAC) World Congress, 2008.

[42] M. Cercignani, D.C. Alexander, Optimal acquisition schemes for in vivo quantitative magnetization transfer MRI, Magn. Reson. Med. 56 (2006) 803–810.

[43] H. Gudbjartsson, S. Patz, The Rician distribution of noisy MRI data, Magn. Reson. Med. 34 (1995) 910–914.

[44] A.H. Andersen, H. Gudbjartsson, S. Patz, On the Rician distribution of noisy MRI data, Magn. Reson. Med. 36 (1996) 331–333.

[45] K.M. Jansons, D.C. Alexander, Persistent angular structure: new insights from diffusion magnetic resonance imaging data, Inverse Probl. 19 (2003) 1031–1046.

[46] J.C. Parker, M.T. van Genuchten, Flux-averaged and volume-averaged concentrations in continuum approaches to solute transport, Water Resour. Res. 20 (1984) 866–872.

[47] M.H.G. Amin, S.J. Gibbs, R.J. Chorley, K.S. Richards, T.A. Carpenter, L.D. Hall, Study of flow and hydrodynamics dispersion in a porous medium using pulsed field gradient magnetic resonance, Proc. R. Soc. London, A 453 (1997) 489–513.

[48] A. Chaudhuri, M. Sekhar, Analytical solutions for macrodispersion in a 3 D heterogeneous porous medium with random hydraulic conductivity and dispersivity, Transp. Porous Med. 58 (2005) 217–241.

[49] N.G. Papadakis, D. Xing, C.L.H. Huang, L.D. Hall, T.A. Carpenter, A comparative study of acquisition schemes for diffusion tensor imaging using mri, J. Magn. Reson. 137 (1999) 67–82.

[50] D.R. Brillinger, Time Series: Data Analysis and Theory, SIAM, 2001.

[51] L. Ljung, Some results on identifying linear systems using frequency domain, in: Proc. 32nd Conf. Decision and Control, San Antonio, TX, 1993.

[52] C.-F. Wu, Asymptotic theory of nonlinear least squares estimation, Ann. Stat. 9 (1981) 501–513.

[53] S.P. Asprey, S. Macchietto, Designing robust optimal dynamic experiments, J. Proc. Cont. 12 (2002) 545–556.

[54] F. Pukelsheim, Optimal Design of Experiments, Wiley, New York, NY, 1993.

[55] T.L. Vincent, B.S. Goh, K.L. Teo, Trajectory-following algorithms for min–max optimization problems, J. Optimiz. Theory Appl. 75 (1992) 501–519.

[56] D. Marquardt, An algorithm for least-squares estimation of nonlinear paramters, SIAM J. Appl. Math. 11 (1963) 431–441.

[57] J.L.R. Andersson, Maximum a posteriori estimation of diffusion tensor parameters using a Rician noise model: why, how and but, NeuroImage 42 (2008) 1340–1356.

[58] L.G. Raguin, S. Majumdar, S. Udpa, Design of optimal experimental parameters for diffusion-weighted MRI fibre-tracking protocols, Int. J. Appl. Electrom. Mech. 28 (2008) 61–67.